

# Hyperspectral and Lidar Intensity Data Fusion: A Framework for the Rigorous Correction of Illumination, Anisotropic Effects, and Cross Calibration

Maximilian Brell, Karl Segl, Luis Guanter, and Bodo Bookhagen

**Abstract**—The fusion of hyperspectral imaging (HSI) sensor and airborne lidar scanner (ALS) data provides promising potential for applications in environmental sciences. Standard fusion approaches use reflectance information from the HSI and distance measurements from the ALS to increase data dimensionality and geometric accuracy. However, the potential for data fusion based on the respective intensity information of the complementary active and passive sensor systems is high and not yet fully exploited. Here, an approach for the rigorous illumination correction of HSI data, based on the radiometric cross-calibrated return intensity information of ALS data, is presented. The cross calibration utilizes a ray tracing-based fusion of both sensor measurements by intersecting their particular beam shapes. The developed method is capable of compensating for the drawbacks of passive HSI systems, such as cast and cloud shadowing effects, illumination changes over time, across track illumination, and partly anisotropy effects. During processing, spatial and temporal differences in illumination patterns are detected and corrected over the entire HSI wavelength domain. The improvement in the classification accuracy of urban and vegetation surfaces demonstrates the benefit and potential of the proposed HSI illumination correction. The presented approach is the first step toward the rigorous in-flight fusion of passive and active system characteristics, enabling new capabilities for a variety of applications.

**Index Terms**—Airborne laser scanning (ALS), deshadowing, imaging spectroscopy, in-flight, mosaicking, pixel-level fusion, preprocessing, radiometric alignment, ray tracing, sensor alignment, sensor fusion.

## I. INTRODUCTION

DATA fusion is a promising approach for producing remote sensing data sets with improved quality and dimensionality. The combination of data from airborne hyperspectral imaging (HSI) sensors and airborne lidar scanners (ALSs) has been previously addressed in [1]–[8]. The particular focus is their complementary sensor characteristics,

Manuscript received October 4, 2016; revised December 19, 2016; accepted January 10, 2017. This work was supported by in part by the The Helmholtz Centre Potsdam, GFZ German Research Centre for Geoscience and in part by “Zentrales Innovationsprogramm Mittelstand” program founded by the Federal Ministry for Economic Affairs and Energy Germany.

M. Brell, K. Segl, and L. Guanter are with the Helmholtz Centre Potsdam, GFZ German Research Centre for Geosciences, 14473 Potsdam, Germany (e-mail: brell@gfz-potsdam.de).

B. Bookhagen is with the Institute of Earth and Environmental Science, University of Potsdam, 14476 Potsdam, Germany.

Color versions of one or more of the figures in this paper are available online at <http://ieeexplore.ieee.org>.

Digital Object Identifier 10.1109/TGRS.2017.2654516

yielding increased data dimensionality and improved classification. The combination of the high spectral resolution of the HSI and the structural information provided by the ALS can yield more complete and improved surface characteristics for a wide range of applications.

Fusion processes are complex, and there are different methods and levels of details to achieve data-type combinations. All approaches rely on an accurate geometric coalignment of both data sources [9]. In general, fusion methods are categorized as either physical or empirical approaches [10]. Physical approaches aim to combine both sensors on a raw data level. Their focus is a parametric representation of particular rigorous sensor models, as well as external conditions. In contrast, empirical approaches combine both data sets based on inherent observable information, without the need for supplementary information. Most approaches, whether physical or empirical, focus on the enhancement of information content by adding the surface elevation information, ALS point classification, and spatial-statistic information as additional dimensions. In addition, physical approaches consider exclusively structural and geometric information [11], [12]. However, ALS systems are not limited to this specific information content. Similar to HSI systems, they also provide intensity information, but usually only for a single ALS wavelength. In contrast, the intensity information is acquired actively and is unfortunately not internally calibrated. Due to the different sensor characteristics, the combination of intensity information is challenging and has often not been taken into account. Several recent studies [13]–[15] systematically compare data from both intensity information sources and note both opportunities and challenges for the adaptation of both sensor responses for heterogeneous surfaces. An overview of the benefits of using the LAS intensity information is given in [16]. Nevertheless, the full use of data from both imaging sensors requires some type of radiometric cross calibration. A cross calibration between HSI and ALS creates a consistent relative radiometric calibration scale, in which the ALS intensities are converted to physical units through comparison with the calibrated HSI data. This process ensures and enhances the temporal, spatial, and spectral comparison of two different sensor systems and is, in addition to the geometric alignment, one of the essential steps for comprehensive data fusion.

The purpose of this sensor fusion is to compensate for solar illumination and atmospheric conditions, as well as directional

TABLE I

NOTATION USED FOR RELEVANT RADIATIVE TRANSFER PARAMETERS

Notation	Explanation	Units
$E_0$	Terrestrial solar irradiance	[W/m <sup>2</sup> ]
$\tau_s$	Atmospheric transmittance sun-surface	[]
$\tau_{atm}$	Atmospheric transmittance surface-sensor	[]
$E_{dir}$	Direct radiation	[W·sr <sup>-1</sup> ·m <sup>-2</sup> ]
$E_{dif}$	Diffuse radiation	[W·sr <sup>-1</sup> ·m <sup>-2</sup> ]
$E_{adj}$	Adjacency radiation	[W·sr <sup>-1</sup> ·m <sup>-2</sup> ]
$L_{HSI}$	Electromagnetic intensity measured by the HSI	[W·sr <sup>-1</sup> ·m <sup>-2</sup> ]
$L_p$	Path radiance	[W·sr <sup>-1</sup> ·m <sup>-2</sup> ]
$\Theta_s$	Solar zenith angles	[deg]
$\beta_{sol}$	Solar incidence angle	[deg]
$\theta_{HSI}$	Viewing angle of the HSI	[deg]
$d$	Relative sun-to-earth distance	[]
$P_t$	Emitted pulse intensity of the ALS	[dB]
$P_r$	Backscattered laser pulse of the ALS	[dB]
$\alpha_{ALS}$	Incidence and viewing angle of the ALS	[deg]

and shadow effects, to derive improved and realistic at-surface reflectance. This is achieved by the rigorous radiometric calibration of the ALS intensity data with the HSI data and the subsequent correction of the amount of direct solar radiation within the atmospheric correction of the HSI data. We have designed and implemented new software for efficient HSI and ALS fusion, with special focus on the radiometric calibration of ALS intensity data and HSI illumination correction. Detailed descriptions of the basics, methodology, results, and discussion are provided in this paper.

## II. BACKGROUND

### A. Radiative Transfer Characteristics

The two sensors have different radiation transfer paths, individual spatial sampling, and sensor characteristics. Therefore, the alignment of different sensor characteristics on a raw level requires a physical radiative transfer-based cross calibration. Fig. 1, in combination with Table I, provides an overview of the different radiative transfer paths and interactions with the exposed surfaces of the two sensor systems.

The atmospheric conditions influencing the measured signals are not the same due to their different atmospheric transfer paths (see Fig. 1). Thus, atmospheric conditions (e.g., cirrus and clouds) above the flight level influence only the HSI transfer path. In addition to cloud shadowing, HSI radiances are influenced by cast shadows, introducing a continuous shadow field exclusively illuminated by diffuse radiation ( $E_{dif}$ ). Compared with direct irradiation, diffuse radiation caused by scattering is not a discrete status and is strongly spectrally variable and dependent. For example, the blue parts of the spectrum are scattered more strongly, and they are thus represented significantly more strongly in the cast shadow [17]. However, lidar intensities are not influenced by the cast shadow due to their active character. This enables active cast shadow detection and correction with a physical approach based on the overlapping wavelength domain and the proportional assignment to the remaining wavelength range of the HSI sensor system.

In general, airborne spectroscopy attempts to identify the true reflectance or absorption property of a surface object at the

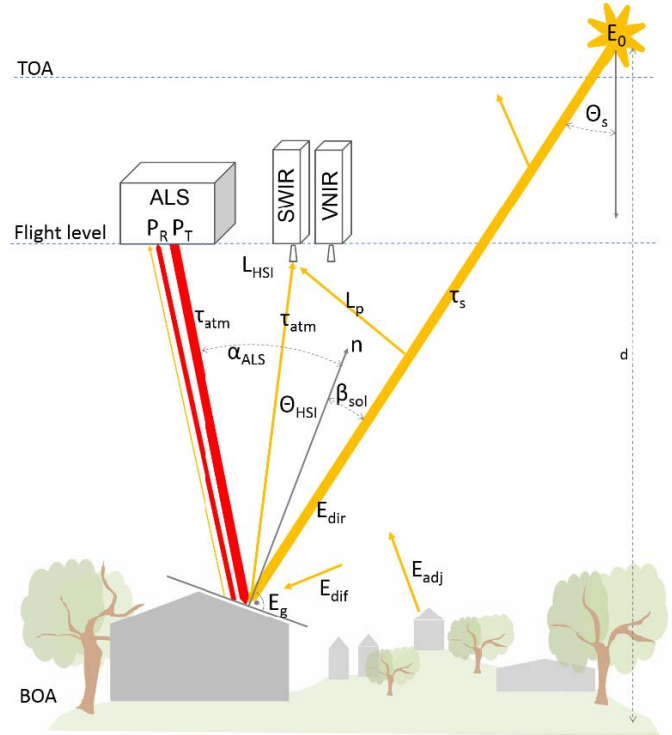


Fig. 1. Conceptualization of the radiative transfer paths of ALS and HSI sensors. See Table I for notation and symbol explanations.

bottom of the atmosphere (BOA). However, the electromagnetic intensity ( $L_{HSI}$ ) measured by HSI sensors is influenced by the solar illumination [terrestrial solar irradiance ( $E_0$ ) and solar zenith angles ( $\Theta_s$ )], its path through the atmosphere (atmospheric transmittance  $\tau_s$ ) starting at the top of the atmosphere (TOA), its incidence angle from the object ( $\beta_{sol}$ ), its path back through the atmosphere ( $\tau_{atm}$ ) to the sensor at flight level, and the resulting path radiance ( $L_p$ ) (Fig. 1). The HSI BOA surface reflectance ( $\rho_{HSI}$ ) of a Lambertian surface can be modeled as

$$\rho_{HSI} = \frac{\pi d^2 (L_{HSI} - L_p)}{\tau_{atm} (E_{dir} + E_{dif})}. \quad (1)$$

The different terms in (1) are listed in Table I. The diffuse radiation ( $E_{dif}$ ) also includes spherical atmospheric albedo reflected from the surface toward the sensor and adjacency radiation ( $E_{adj}$ ). The direct radiation ( $E_{dir}$ ) can be calculated by

$$E_{dir} = E_0 \tau_s \cos \Theta_s. \quad (2)$$

In addition, surface roughness and anisotropic object properties are also relevant for the radiative transfer.

Without geometric and morphometric information of the surface object, HSI data can be corrected only to Lambertian-equivalent reflectance, where directional effects and shadows are not taken into account.

Alternately, a large advantage of ALS data is that the surface normal ( $n$ ) of an object surface can be calculated by the analysis of neighboring point measurements, enabling the reconstruction of the incidence angle of the laser pulse. This circumstance can also be exploited within the radiometric calibration of ALS intensity data. Several studies devote

themselves to the absolute radiometric calibration of ALS data [18]–[20], and a review of lidar radiometric processing is given in [21]. Most approaches rely on the basic lidar equation and substitution of unknown terms with ground-based *in situ* reflectance measurements

$$P_r = \frac{P_t D_r^2}{4\pi R^4 \beta_t^2} \tau_{sys} \tau_{atm} \sigma. \quad (3)$$

In general, the measured backscattered laser intensity is analogous to HSI systems influenced by sensor parameters, atmospheric conditions, and surface properties. The backscattered laser pulse ( $P_r$ ) is the result of the emitted pulse intensity ( $P_t$ ) and its direction, range ( $R$ ) or path through the atmosphere and return, its atmospheric transmittance ( $\tau_{atm}$ ), and the effective target cross section ( $\sigma$ ) considering the incidence angle ( $\alpha_{ALS}$ ). Sensor-dependent parameters [e.g., the beam width angle ( $\beta_t$ ), receiver aperture size ( $D_r$ ), and system transmittance factor ( $\tau_{sys}$ ) describing sensor specific attenuation, such as the transmittance efficiency, and sensitivity of the detector] and basic sensor specifications (e.g., wavelength, bit depth, multiple returns/full waveform, an amplifier for low-reflectivity surfaces, attenuation for near targets, and automatic gain control) are required. Additional overall influential factors are solar background radiation and the size, angle of incidence, roughness, and wetness of the illuminated surface. Usually, the emitted pulse intensity, some sensor parameters, and the atmospheric conditions are unknown. Rigorous approaches assume that these parameters are constant over the entire flight campaign. Thus, they can be represented by a calibration constant ( $C_{cal}$ ), which can be estimated by *in situ* reflectance measurements [12], [19]. Based on the lidar equation (3) for every return signal, the backscatter coefficient ( $\gamma_i$ ) can be calculated. The backscatter coefficient is independent of range ( $R$ ) and beam divergence ( $\beta_t$ ) because it is normalized to the laser's transverse area [18], [19].

### III. METHODOLOGY

The proposed approach is the first step toward an in-flight physically based fusion of airborne radiometric measurement capabilities by combining an active ALS sensor with a passive HSI sensor. Most of the influential parameters are wavelength dependent, and the overlapping wavelength domain thus defines the comparability of the sensor responses. The data fusion is performed by intersecting the pointing of a HSI sensor element, represented by a cone, with the ALS point cloud. Hence, the complete set of ALS point properties inside one HSI beam can be accessed and adequately adapted, considering the full radiometric and structural information.

The complete in-flight radiative transfer-based cross calibration of the ALS and HSI intensity signal can be split into three principal parts (see Fig. 2):

- 1) input data acquisition and preprocessing (including the geometric coalignment of the sensors);
- 2) cross calibration and BOA reflectance calculation;
- 3) output data generation.

#### A. Input Data Generation and Preprocessing

For the purpose of developing the in-flight sensor fusion, a test data set with a specially adapted measurement setup,

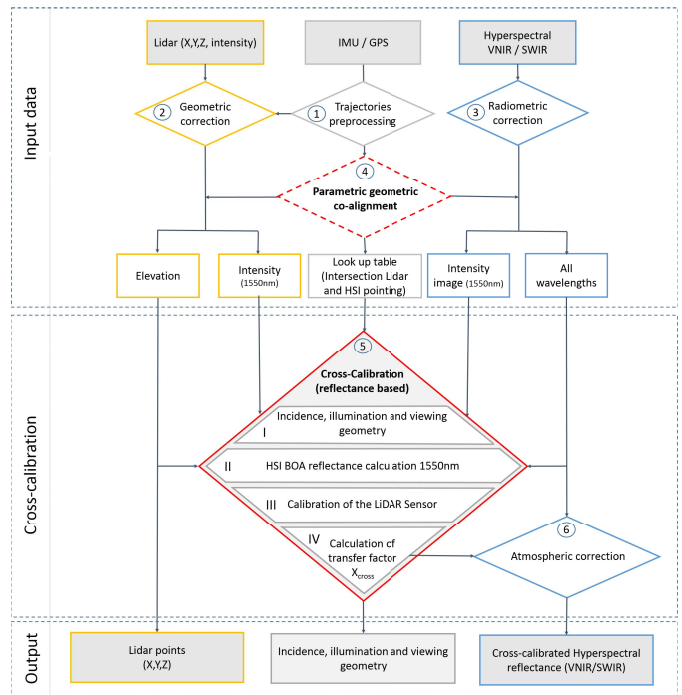


Fig. 2. Overview of the simplified cross-calibration workflow (rectangles represent data products; processing procedures are represented by rhombs; yellow outlines indicate steps applied to ALS data only; blue outlines indicate steps used for HSI data only; gray outlines indicate levels associated with both datasets; and central fusion steps are outlined in red).

sensor operation, and flight planning was generated. In addition to the HSI system, consisting of two HySpex sensors (VNIR-1600 and SWIR-320m-e [22], [23]), an ALS (LMS-Q560 [24], [25]) and an IMU/GPS (AEROcontrol-II) IMU in combination with a NovAtel OEM4-G2 GPS) for measuring the position and attitude of the airplane were integrated inside a Cessna 207 Skywagon. Table II gives an overview of the HSI and ALS specifications.

Four flight lines were acquired at an altitude of 800 m above the ground over an airfield with bordering suburban development in Kamenz, Germany (51.29063°N 14.12107°E). The acquired suburban objects (buildings, roads, trees, fields, and moving objects) represent a radiative as well as a morphometrically diverse test site. The achieved ground sampling distances of approximately 1.2 m for SWIR and 0.6 m for VNIR, as well as a point density of approximately 5 points/m<sup>2</sup> delivered by the ALS in nonoverlapping areas, sufficiently represent the spectral and morphological surface heterogeneity. The HSI test data are strongly influenced by cloud shadows and cast shadows that limit any HSI analysis [Fig. 3(a)]. Accordingly, this test site represents an ideal benchmark to show the capabilities and limitations regarding the fusion of active and passive system characteristics.

In addition to the elevation information, ALS range, amplitude, and echo width are provided to meet the requirements of the proposed method. For state-of-the-art full-waveform ALS systems, these attributes are easily accessible.

The full-waveform ALS, the IMU/GPS measurement unit, and the HSI (VNIR and SWIR) provide the input database. The preprocessing includes the calculation of trajectories (see rhomb 1 in Fig. 2), the geometric preprocessing of the

TABLE II  
COMPARISON OF RELEVANT SENSOR PARAMETERS

	VNIR and SWIR HSI (Hypex)	ALS (LMS-Q560)
Principle	passive	active
Sensor design	Pushbroom	Whiskbroom (polygon mirror)
FOV (Field of View)	VNIR: 35.5° SWIR: 27.2°	45° (up to 60°)
IFOV (instantaneous field of view)	VNIR: across track 0.18 mrad along track 0.36 mrad SWIR: across track 0.75 mrad along track 0.75 mrad	-
Laser beam divergence		< 0.3 mrad
FWHM (spectral)	VNIR: 1.0-2 pixels SWIR: 1.5-2 pixels	
Spectral range	VNIR: 400 - 1000 nm SWIR: 1000 - 2500 nm	1550 nm (Laser class 1)
Frames per second (HSI) Pulse frequency (ALS)	VNIR: 135 fps SWIR: 100 fps	240 kHz (160 lines/s)
Spectral sampling	VNIR: 3.7 nm SWIR: 6 nm	monochromatic
Pulse length		< 4 ns at half maximum
Echo sampling interval		Full-waveform (1 ns)
Intensity digitization	12 bit	16 bit
Spectral bands	VNIR: 160 SWIR: 256	1
Spatial pixels HSI	VNIR: 1600 SWIR: 320	

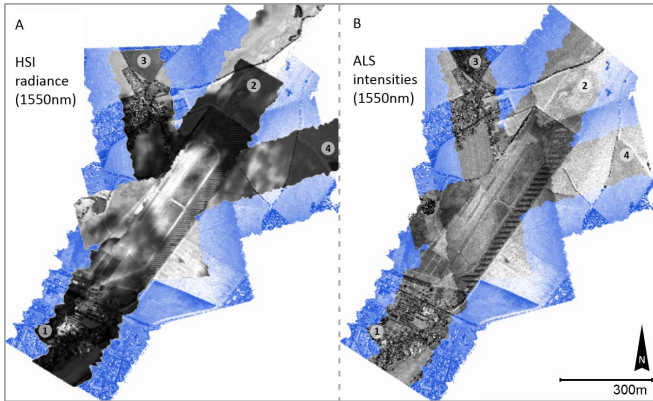


Fig. 3. Overview of the four geocoded flight lines (1–4); HSI footprint colored in black and ALS footprint colored in blue. (a) HSI SWIR radiance image (1550 nm). (b) ALS intensity image (1550 nm).

ALS data including filtering of outliers and ALS returns introduced by atmospheric interactions (see rhomb 2 in Fig. 2), and the radiometric correction of the HSI data (see rhomb 3 in Fig. 2). In addition, the cross calibration requires a proper geometric coalignment of the HSI intensity information with the ALS point cloud. This coalignment of the HSI sensor data to the ALS data is created with a parametric approach using the adapted ALS intensity information as a geometric reference. The applied approach is described in detail in [9] and also includes a detailed description of the necessary spectral response adaptation [26], system integration, data acquisition, and preprocessing. The ray tracing-based approach delivers a subpixel coalignment in heterogeneous urban areas, as well as a lookup table for all ALS points that intersect a particular HSI beam.

#### B. Cross-Calibration Procedure

As shown in Fig. 2 (rhomb 5), the cross calibration itself is implemented in four major steps:

- 1) calculation of incidence, illumination, and viewing

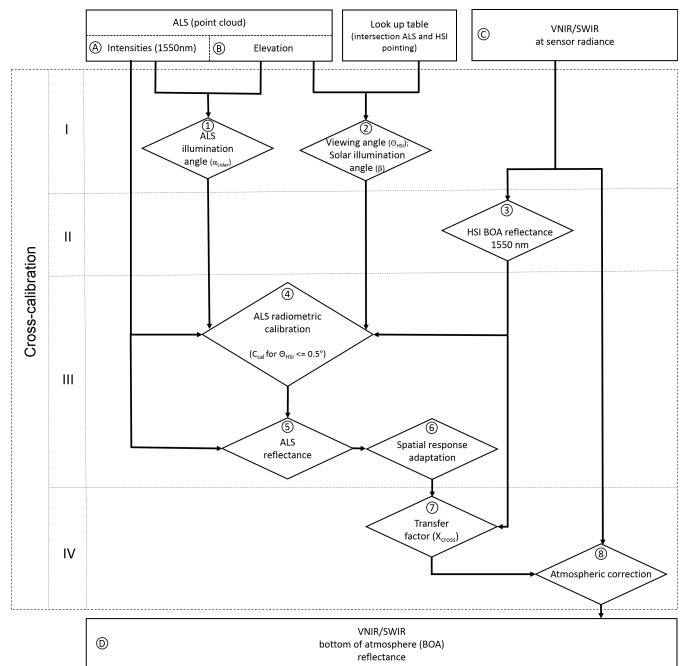


Fig. 4. Detailed workflow of the four cross-calibration steps. Rectangles represent (a)–(d) input and output data products. Rhombs represent (1)–(8) applied processing modules.

geometry for both sensors;

- 2) calculation of HSI BOA reflectance at 1550 nm;
- 3) radiometric calibration of the ALS sensor;
- 4) calculation of the transfer factor ( $X_{\text{cross}}$ ) and HSI BOA reflectance.

**1) Calculation of Incidence, Illumination, and Viewing Geometry for Both Sensors:** The calculation of the incidence, illumination, and viewing geometry is the first step in the cross-calibration workflow [see Fig. 4(1)]. The ALS incidence angles ( $\alpha_{\text{ALS}}$ ), solar illumination angles ( $\beta_{\text{sol}}$ ), and HSI viewing angles ( $\Theta_{\text{HSI}}$ ) are essential to characterize the interaction between the sensors and the sun with the local surface (see Fig. 1). In general, the calculation of the angles is carried out by a ray tracing-based intersection of the sensor beams with the local surface model.

The ALS incidence angle [Fig. 6(1)] is calculated in a first step by intersecting each ALS beam with its neighboring ALS beams. The ALS beam is defined by its beam divergence, the position of the transmitter, and the position of the surface target. A least squares approach fits a plain through all points that fall into one ALS beam. For every plain representing the local underlying surface that is intersected by an ALS beam, the surface normal is calculated. The angle between this ALS beam and the surface normal represents the ALS incidence angle ( $\alpha_{\text{LIDAR}}$ ).

For the calculation of the solar illumination angles ( $\beta_{\text{sol}}$ ) [see Fig. 6(2)], the surface intersected by the HSI beams and their surface normal are calculated with the same procedure used for the calculation of the ALS incidence angle. The viewing angles [ $\Theta_{\text{HSI}}$ ; see Fig. 6(3)] between the HSI beams and the surface normal are calculated, as well as the terrain slope angle ( $\Theta_T$ ) and the topographic azimuth angle ( $\varphi_T$ ). In addition, the solar azimuth ( $\varphi_s$ ) and solar zenith angles ( $\Theta_s$ )

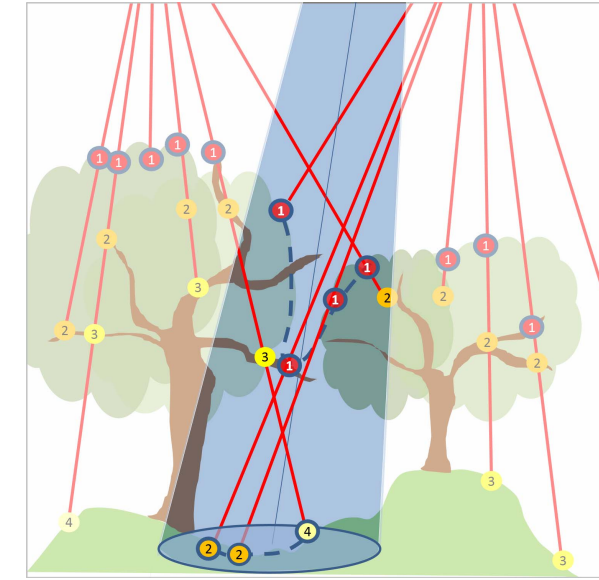


Fig. 5. Interaction between the canopy, ALS pulses (red lines; returns are indicated with numbered dots), and HSI beam (blue beam); blue outlined dots are used to build the reflectivity information representing the corresponding HSI information; blue dashed lines inside the HSI cone represent the two return levels integrated into the reflection representation of this HSI cone.

are calculated based on the acquisition date and the position. By applying all these angles, the solar illumination angle is given for every HSI beam [27]

$$\beta_{\text{sol}} = \arccos(\cos \Theta_T \cos \Theta_s + \sin \Theta_T \sin \Theta_s \cos(\varphi_T - \varphi_s)). \quad (4)$$

2) *HSI Bottom of Atmosphere Reflectance Calculation* [Fig. 4(3)]: For the radiometric calibration of the ALS, the HSI BOA reflectance must be known for the overlapping wavelength domain (1550 nm). Therefore, the TOA HSI radiance data cube is transformed to BOA reflectance (Fig. 2, rhomb 5 II). This atmospheric correction is realized with in-house correction algorithms [26], [28], based on the radiative transfer code MODTRAN4 [29]. Thereby, the BOA surface reflection ( $\rho_{\text{HSI}}$ ) is calculated with the standard formulas (1) and (2). Shadows and rough terrain are not considered in this correction step [Fig. 6(3)].  $\rho_{\text{HSI}}$ ,  $E_{\text{dir}}$ , and  $E_{\text{dif}}$  are provided separately for the overlapping wavelength domain (1550 nm), to enable the subsequent calculation of  $X_{\text{cross}}$ .

3) *ALS Radiometric Calibration* [Fig. 4(4)]: The calculated HSI reflectance from the previous processing step is now used for the calibration of the ALS intensity signal applying the calibration constant ( $C_{\text{cal}}$ ) [18]–[21]. Based on the lidar equation and the use of the backscatter coefficient ( $\lambda_i$ ) [19], the surface reflectance  $\rho_{\text{ALS}}$  can be directly calculated

$$\rho_{\text{ALS}} = C_{\text{cal}} \frac{R^2 P_r}{\tau_{\text{atm}} \cos \alpha_{\text{ALS}}^4}. \quad (5)$$

The constant sensor parameters are combined into one calibration constant ( $C_{\text{cal}}$ )

$$C_{\text{cal}} = \frac{16}{P_t D_r^2 \tau_{\text{sys}}}. \quad (6)$$

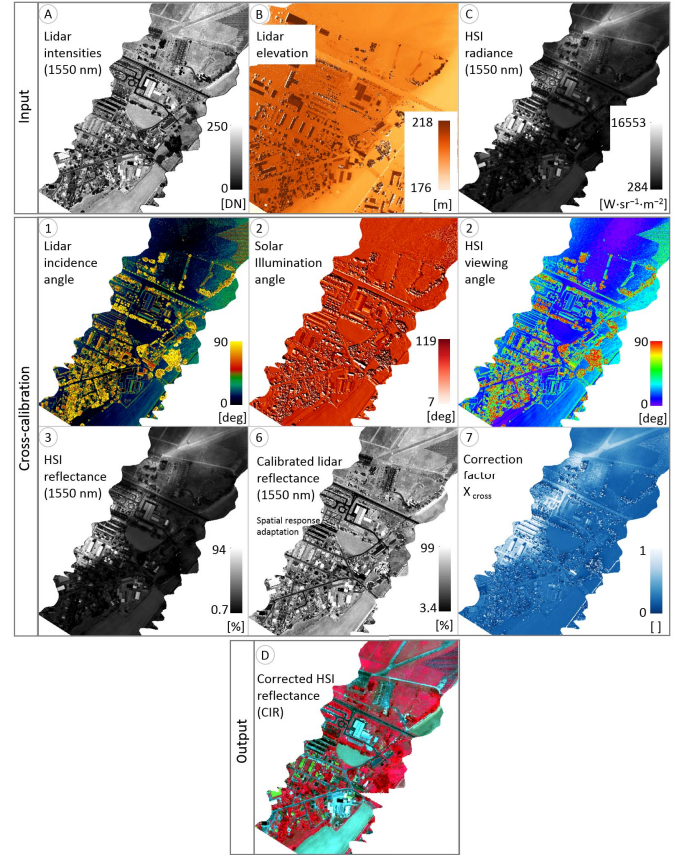


Fig. 6. Geocoded overview of the (a)–(d) input/output data products and results of the (1)–(7) processing modules using nonconsecutive numeration corresponding to the detailed workflow diagram (Fig. 4).

To determine the calibration constant ( $C_{\text{cal}}$ ), we solve (8) for  $C_{\text{cal}}$

$$C_{\text{cal}} = \frac{\rho_{\text{ALS}} \tau_{\text{atm}} \cos \alpha_{\text{ALS}}^4}{R^2 P_r}. \quad (7)$$

Several approaches (see [18], [19]) substitute  $\rho_{\text{ALS}}$  with *in situ* reflectance measurements to determine  $C_{\text{cal}}$ . Instead of an empirical calibration based on the *in situ* reflectance measurements of surface targets, our approach aims to create an in-flight cross calibration with the wavelength overlapping HSI sensor. The criteria for every HSI beam include that the calibration surface is a homogeneous target that can be assumed to be a Lambertian reflector representing stable radiation conditions and that it is not influenced by shadows. For the test data, which are strongly influenced by cloud shadows, an area of interest (AOI) was manually defined that covers the directly illuminated part of the runway. Within this AOI, only HSI beams were selected automatically, which have viewing angles  $\Theta_{\text{HSI}} \leq 0.5^\circ$ , intersect at a minimum with five ALS points, and have incidence angles  $\alpha_{\text{ALS}} \leq 0.5^\circ$ .

The requirement for substituting  $\rho_{\text{ALS}}$  with  $\rho_{\text{HSI}}$  in (7) is that the spatial response of the ALS sensor must be adapted to the spatial response of the HSI sensor. Therefore, ALS points that fulfill the mentioned criteria and intersect with the selected HSI beams are spatially adapted. The spatial response adaptation is described in Section III-BIII-B.4. Therefore, both

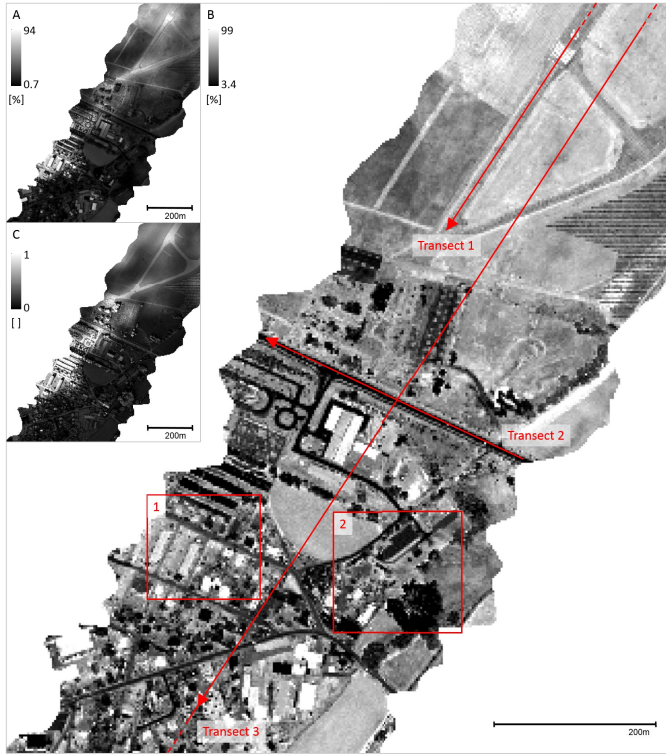


Fig. 7. Overview of one corrected flight line of 1550 nm, with red marked subsets and profiles used for further accuracy assessment. (a) HSI BOA reflectance of 1550 nm (no shadow correction). (b) HSI BOA reflectance of 1550 nm (all corrections applied). (c) Correction factor  $X_{\text{cross}}$  calculated for the atmospheric transformation to all HSI wavelengths.

sensor responses can be regarded as analogous at this point. This adaptation is created for all HSI beams ( $N_{\text{HSI}}$ ) that satisfy the mentioned criteria to calculate the mean calibration constant  $C_{\text{cal}}$

$$\overline{C}_{\text{cal}} = \frac{1}{N_{\text{HSI}}} \sum_{j=1}^{N_{\text{HSI}}} \frac{\pi d_j^2 (L_{\text{HSI}_j} - L_{P_j}) \cos \alpha_{\text{ALS}_j} 4}{(E_{\text{dir}_j} + E_{\text{dif}_j}) R_j^2 P_{r_j}}. \quad (8)$$

Using  $\overline{C}_{\text{cal}}$  for the radiometric calibration of the ALS intensities within (5) results in cross-calibrated ALS reflectances [Fig. 4(5) and Fig. 6(6)].

a) *Spatial response adaptation of ALS points:* To compare both sensor signals, the cross-calibrated intensity signal of the ALS point cloud has to be adapted spatially, considering the point spread function (PSF) of the HSI sensor [Fig. 4(6)]. It is created with a ray tracing-based approach intersecting the HSI cones with the ALS point cloud. The received ALS signal ( $P_r$ ) is weighted relative to its distance to the cone center with a Gaussian PSF centered along the center axis of the HSI cone. A detailed description of the spatial response adaptation is given in [9]. With this method, the spatial response function is correctly approximated regarding the spatial footprint projection and orientation. All calculations are realized in SWIR sensor geometry (Fig. 10) and backprojected to ALS points and VNIR data. This strategy avoids the resampling of the HSI data and thus the associated degradations.

Due to the ray tracing-based intersection approach, a filtering and an adaptation of the point cloud are created separately for every single HSI beam. The discrete return intensities

are filtered based on their elevation variance inside one HSI beam (Fig. 5). Every time the elevation variation inside an HSI beam exceeds a threshold, the variance is minimized by separating the point cloud into two continuous surfaces by histogram filtering. This approach results in two continuous surface representations: the ALS points representing higher regions in the canopy and the bare ground points. Only if sparse first pulse returns and dense higher order returns are detected inside one HSI beam, the higher order returns are also considered in the sensor response adaptation (Fig. 5).

This procedure accounts for the attenuation correction in the surroundings of dense vegetation where sparse vegetation splits the ALS energy into multiple returns (Fig. 5). For HSI beams with dense first pulse returns caused by the canopy and sparse returns of higher order inside or underneath the vegetation, the top first pulse returns are used to build a continuous surface. Only these top first pulses represent the canopy parts influencing the area integrating the sensor answer of the HSI system.

4) *Calculation of the Transfer Factor  $X_{\text{cross}}$ :* For the transfer of the cross calibration between the overlapping wavelength domain of 1550 nm [Fig. 4(7)] and the remaining wavelength, an additional factor ( $X_{\text{cross}}$ ) is introduced into (1).  $X_{\text{cross}}$  is intended to represent differences in illumination between shaded and fully illuminated areas. In fully illuminated areas,  $E_{\text{dir}}$  and  $E_{\text{dif}}$  are present. In shaded areas,  $E_{\text{dir}}$  is absent, and only  $E_{\text{dif}}$  is present. Thus,  $X_{\text{cross}}$  adjusts the amount of  $E_{\text{dir}}$  based on the calibrated and adapted ALS intensity data. Therefore, (1) with the introduced factor  $X_{\text{cross}}$  is solved by substituting  $\rho_{\text{HSI}}$  for 1550 nm with the cross-calibrated ALS reflectance ( $\rho_{\text{ALS}}$ )

$$X_{\text{cross}} = \frac{\pi d^2 (L_{\text{HSI}} - L_{\text{PHSI}})}{E_{\text{dir}} * \rho_{\text{ALS}} * \tau_{\text{atm}}} - \frac{E_{\text{dif}}}{E_{\text{dir}}}. \quad (9)$$

The determined factor  $X_{\text{cross}}$  [Fig. 6(7)] is then used to calculate  $\rho_{\text{HSI}}$  for all remaining wavelengths. This results in corrected HSI reflectance [Fig. 6(d)].

5) *Requirements and Assumptions:* Considering the following four requirements and assumptions, the presented generic method can be applied to the complete flight campaign, as well as to other system configurations and characteristics. First, one of the main prerequisites for the cross calibration is an accurate spectral and geometric coalignment, which includes the adaptation of the overlapping wavelength domain considering the central wavelength and bandwidth. Second, it has to be assumed that both sensor systems are geometrically and radiometrically stable during the entire flight campaign. Third, the characteristic of the laser pulse regarding amplitude, echo width, and shape of the reflected echo should be known. Thus, the complexity of the underlying object reflection is fully represented, and a radiometric correction is also possible for nonhorizontal targets [19]. Consequently, the detection of return echoes and the separation into different reflections out of the full-waveform information can be created with Gaussian decomposition [19], [25]. Fourth, the approaches for the radiometric calibration of ALS intensities assume that all surface objects diffusively reflect according to the Lambertian law. This assumption

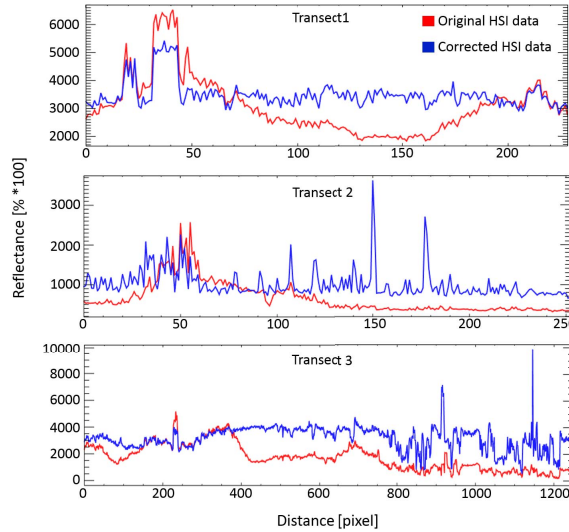


Fig. 8. Along- and across-track transects representing reflectance for 1550 nm (red uncorrected and blue corrected),  $x$ -axis represent the underlying pixel ( $1.2 \times 1.2$  m), (Transect 1) along track intersecting the concrete runway, (Transect 2) across track intersecting asphalt road, and (Transect 3) along track intersecting various surface materials.

enables the calculation of diffuse reflectance, which depends only on the object properties, not on the viewing angle.

#### IV. RESULTS

The introduced radiometric cross calibration generates an HSI reflectance data cube with reduced shadowing and illumination influences. In the following, these results are presented and evaluated for the test data set, which is strongly influenced by illumination effects. The chapter is divided into a comparison of the adapted intensity information of the overlapping wavelength domain of 1550 nm, an investigation of the corrected HSI data cube, and an evaluation of the potentials for HSI data quality and classification improvements.

##### A. Comparison Between the Overlapping Wavelength Domain of 1550 nm

A rough visual comparison between the standard reflectance results for HSI [Fig. 7(a)] and the reflectance calculated based on the cross-calibration approach [Fig. 7(b)] for the wavelength domain of 1550 nm clearly shows the successful correction of illumination influences in the HSI-ALS fused data. Despite the complex illumination situations caused by cloud shadowing, low solar elevation, and heterogeneous object exposure, the correction appears consistent thanks to the radiometrically calibrated active ALS signal.

A closer inspection of the reflectance (1550 nm) based on three transects [marked in Fig. 7(b) with red arrows] confirms the consistency. Transect 1 (Fig. 8) indicates the impact of the cross calibration to the reflectance values representing the concrete runway in the along-track direction of the flight stripe. Compared with the uncorrected reflectance values (red plot), the blue plot alternates at a constant level of approximately 30% reflectance. The high frequency contrast between the pixels is preserved or enhanced due to a higher signal level, whereas the low frequency contrast introduced by illumination differences is compensated for. The same is valid for transect 2

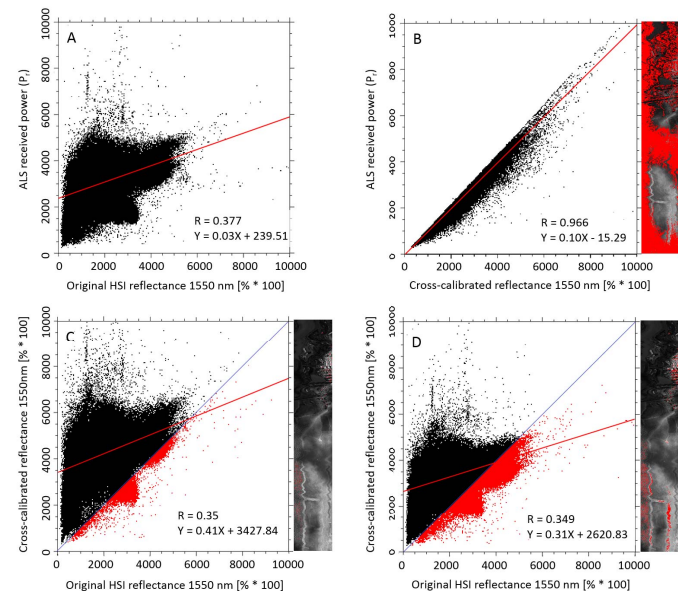


Fig. 9. Various scatter plots indicating the relationship between ALS data and HSI data in the overlapping wavelength domain of 1550 nm. (a) Relation between original HSI data ( $x$ -axis) and ALS received power ( $y$ -axis). (b) Relation between the cross-calibrated data ( $x$ -axis) and uncorrected ALS received power ( $y$ -axis). (c) and (d) Influence of different calibration targets [(c) runway and (d) grass] and their overall nonlinear relation between original HSI data ( $x$ -axes) and cross-calibrated data ( $y$ -axes). The blue reference lines ( $x = y$ ) separate the data sets into two parts: black clusters represent pixels that have expectedly higher values after the cross calibration; red clusters represent pixels that have smaller values after cross calibration; and the spatial distributions of the red clusters are shown in the flight stripes on the right.

at a lower reflectance level of approximately 8%, representing the across-track influence intersecting a relatively homogeneous asphalt road. Additional spikes become apparent due to moving cars and retroreflective lane markings not represented equivalently in both sensor responses. Transect 3 extends in the along-track direction over the complete flight stripe representing its inherent heterogeneity. This transect confirms the results of transects 1 and 2.

The two scatter plots in Fig. 9(a) and (b) show the relation between the received ALS power ( $P_r$ ) ( $y$ -axis) and reflectance ( $x$ -axis) for the original HSI reflectance [Fig. 9(a)] and cross-calibrated HSI reflectance [Fig. 9(b)]. The regression lines (in red) and their equation ( $y$ ), as well as the Pearson correlation coefficient ( $R$ ), are presented. Fig. 9(a) depicts highly uncorrelated information due to the different illumination conditions and differences in the sensor response. However, after the cross calibration, a close-to-linear relationship is observed [Fig. 9(b)]. As expected, the spatial distribution of the nonlinear values [under the regression line marked in red Fig. 9(b, right)] has no correlation with solar illumination conditions. The differences between radiometrically uncorrected ALS intensities and cross-calibrated intensities due to varying ALS point density and overall surface heterogeneity become apparent. It highlights the indispensability of the radiometric calibration of the ALS data.

Scatter plots (C) and (D) represent the relations between the original HSI ( $x$ -axes) and the cross-calibrated ( $y$ -axes) reflectance for two different calibration targets. Plot (C) results

from the calibration on selected pixels from the runway and (D) from grassland. Both plots also show that the relation between ALS and HSI is highly uncorrelated and affected by noise due to the differences of the respective radiation paths and the interaction with the surface objects. Red marked clusters separated by the blue reference line ( $x = y$ ) indicate pixels with unrealistically smaller values after the cross calibration. Their spatial distribution is also shown in the flight lines on the right side. In addition to complex anisotropic surface behavior (e.g., solar array and sheet-metal roofing), the smaller values result from a small overestimation of the first HSI reflectance calculation [Fig. 4(3)] caused by an underestimation of complex diffuse illumination conditions inside small gaps in the clouds. Fig. 9(c) and (d) indicates that the different reflectance characteristics of grassland and concrete due to anisotropy and roughness generate differences in the sensor responses of the two sensors. It is caused by the fact that the calibration targets do not strictly fulfill the requirements of a Lambertian surface, and thus both sensor systems still have a surface-dependent characteristic difference in their sensor responses. Also Fig. 7(c) representing the correction factor  $X_{\text{cross}}$  does not change only with direct illumination variation. Different anisotropy and roughness characteristics of the different surfaces are still apparent in the factor. Nevertheless, it is assumed that the runway most likely fulfills the Lambertian surface criteria and serves as the final cross-calibration target for all further results. This target sensitivity not only highlights the relative character of the cross calibration but also emphasizes the opportunity to optimize for different surface characteristics.

### B. Corrected HSI Data Cube

The spatial pattern of the derived correction factor ( $X_{\text{cross}}$ ) shown in Fig. 7(c) is used to compensate for the unwanted illumination patterns for the remaining wavelength of the HSI sensors. The result of this proposed transformation is shown in Fig. 10(b) in comparison with the uncorrected HSI reflectance [Fig. 10(a)]. The visual comparison indicates the overall good performance of the method. The patterns of illumination differences that are clearly visible in the HSI reflectance data [Fig. 10(a)] are eliminated without any recognizable artifacts in the transition zones. This fact is also confirmed by the comparison of the selected spectral profiles (Fig. 10, middle). The first spectral comparison of the grassland surface (1) shows that the corresponding spectra are nearly identical before and after the correction. This is due to illumination by direct and diffuse radiation without the influence of shadows. All other example spectra are influenced by shadows (red spectra in 2–5), exhibiting a clear attenuation. They are located in areas where only diffuse illumination exists, which is not considered in (9). After the correction, the spectra (blue spectra in 2–5) indicate that this lack of direct illumination is compensated for, and the spectra are raised to plausible reflectance values.

Fig. 11(a) and (b) shows the spatial pattern of the cross-calibration-induced reflection modification by two difference images calculated for two different wavelengths 549.3 nm [Fig. 11(a)] and 1651.8 nm [Fig. 11(b)]. Both images demonstrate the correction of the illumination conditions. However, differ-

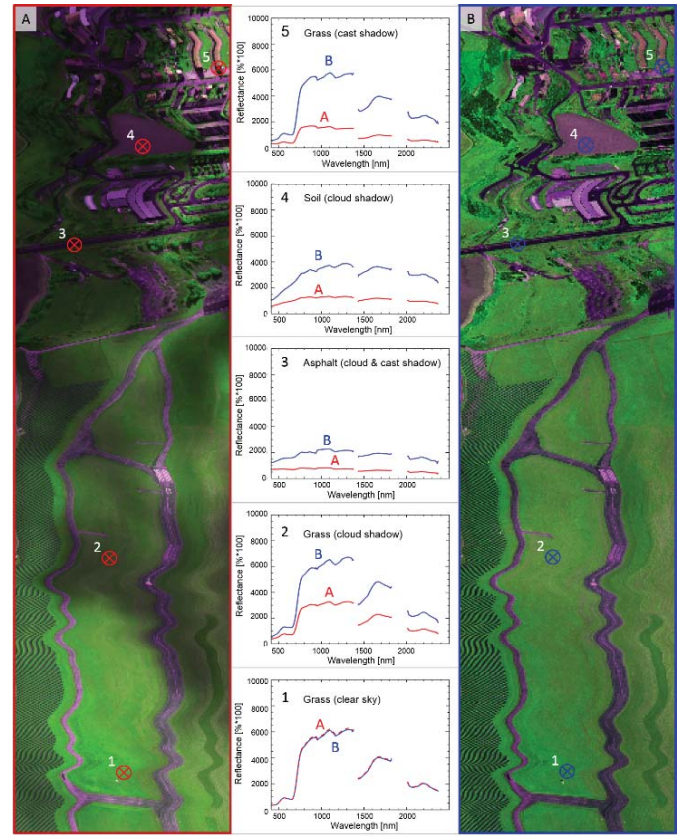


Fig. 10. Atmospheric corrected HSI reflectance (backprojected to SWIR sensor geometry;  $R = 702 \text{ nm}$ ,  $G = 1249 \text{ nm}$ , and  $B = 586 \text{ nm}$ ). (a) Without cross calibration (red label). (b) Cross-calibrated corrected data (blue label). Middle: comparison of uncorrected (a) and corrected (b) reflectance spectra for (1)–(5) different surface materials influenced by various illumination conditions.

ent surface objects are also visible in homogeneous illuminated areas. This can be explained by small illumination and viewing differences caused by surface roughness and anisotropic behavior. Despite the sensor adaptation, these effects, which influence the sensor responses, are still inherent in the data.

### C. HSI Data Quality and Classification Improvements

A detailed visual comparison of subsets 1 and 2 (red boxes in Fig. 7) is presented in Fig. 12. It is clearly visible that the illumination influence inherent in the original HSI data [red border in Fig. 12(a) and (d)] is corrected [blue border in Fig. 12(b) and (e)] without any visual artifacts in the transition areas. This circumstance is also confirmed by the difference images [Fig. 12(c) and (f)] where the transition between directly illuminated areas and cast shadow areas, as well as cloud shadow areas, is very smooth and reasonable. The correction of the solar illumination influence is especially visible at saddle roofs exposed on one side toward the sun, and on the other side, only diffuse radiation is present. In Fig. 12(b), these patterns are entirely compensated for. Fig. 12(e) indicates that the shadow influencing the canopy representation of the large tree can also be compensated for. All of this indicates the potential of the proposed method, especially for advanced vegetation and canopy studies [4], [30], [31], as well as for urban mapping [5], [32].

Overall, it is perceptible that the internal contrast inside homogeneous areas, for example, the asphalt road [Fig. 12(b)]

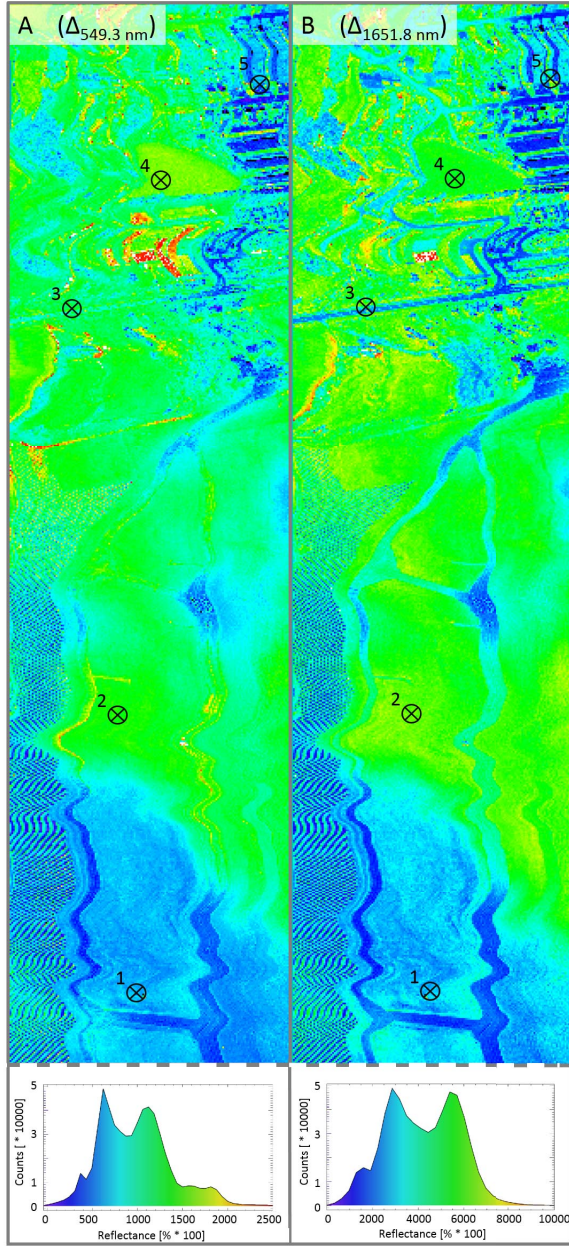


Fig. 11. Reflectance difference ( $\Delta$  = cross-calibrated reflectance-original HSI reflectance) between adjacent wavelength with their respective color slices and histograms for (a) 549.3 and (b) 1651.8 nm. Locations of reflectance spectra shown in Fig. 10 are marked with black crosses.

or the field [Fig. 12(e)], is enhanced. However, the difference images [Fig. 12(c) and (f)] indicate relatively homogenous internal patterns for these regions. These enhancements can be explained by contrast stretching due to the elimination of shadow information. Artifacts or structures that are not visible in the original HSI data are not generated. Thus, the cross calibration enhances the local contrast, but does not add inherent ALS speckle to the results. It seems that the spatial sensor adaptation (Section III-BIII-B.4) successfully suppresses such artifacts.

One of the benefits of the cross calibration is its inherent interflight stripe adjustment. It results in a seamless mosaic [Fig. 13(b)] with a remarkable reflectance match in the overlapping pixels [Fig. 13(1)–(4)]. Despite the data acquisition not

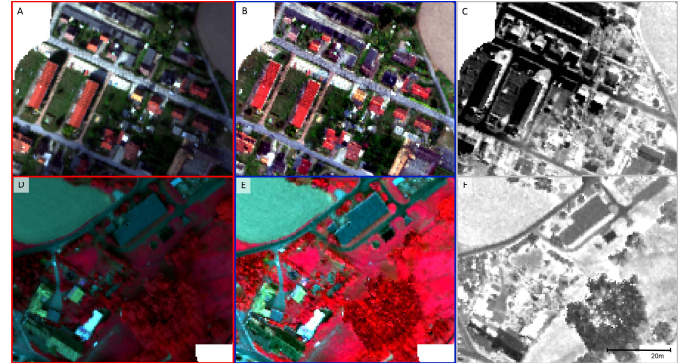


Fig. 12. Detailed comparison of the fusion procedure, and all images are displayed with 1% linear global stretch. (a) Uncorrected HSI reflectance image (RGB) transition zone between direct illumination and cloud shadow. (b) Corrected HSI reflectance image (RGB) without any illumination artifacts. (c) Grayscale difference images [(a) and (b)] indicating areas with less (black) and strong (white) solar illumination influence; the same for (d)–(f), except for displaying CIR false color for (d) and (e).

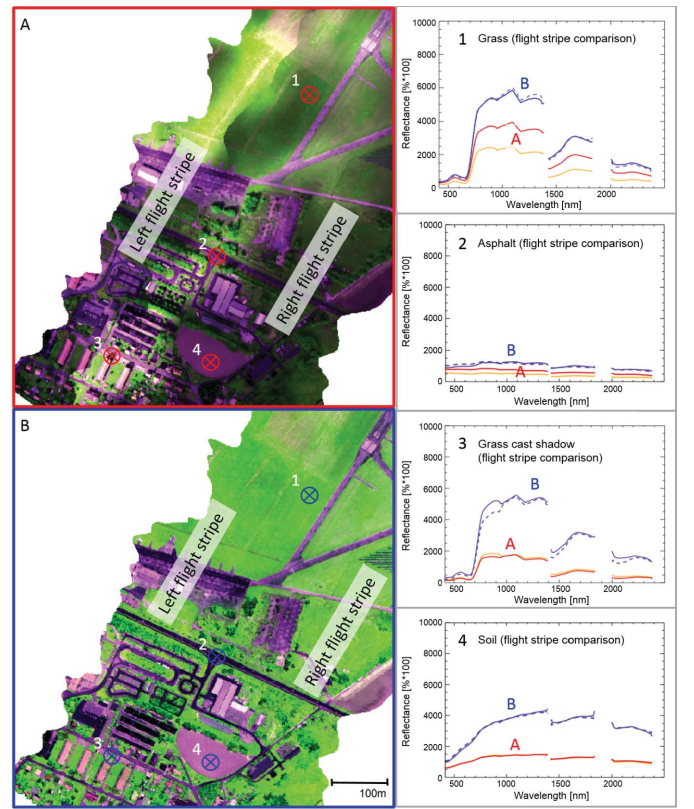


Fig. 13. Spectral comparison between two adjacent and overlapping flight stripes. (a) Uncorrected HSI reflectance. (b) Corrected HSI reflectance. (1)–(4) Sample spectra from overlapping pixels (orange and violet = spectra of left flight strip, and red and blue = spectra of right flight strip).

being perpendicular to the solar principal plane, across-track illumination gradients are not observed [Fig. 8, transect 2, and Fig. 13(b)]. The modifications caused by the cross calibration and their spatial, radiometric, and spectral characteristics are also visible in Fig. 14, where the differences between the two overlapping adjacent flight stripes are analyzed for two wavelengths [549.3 nm in Fig. 14(a) and (c) and 1651.8 nm in Fig. 14(b) and (d)]. The differences for the uncorrected reflectance [red border in Fig. 14(a) and (b)] show strong illumination patterns. However, the differences between the

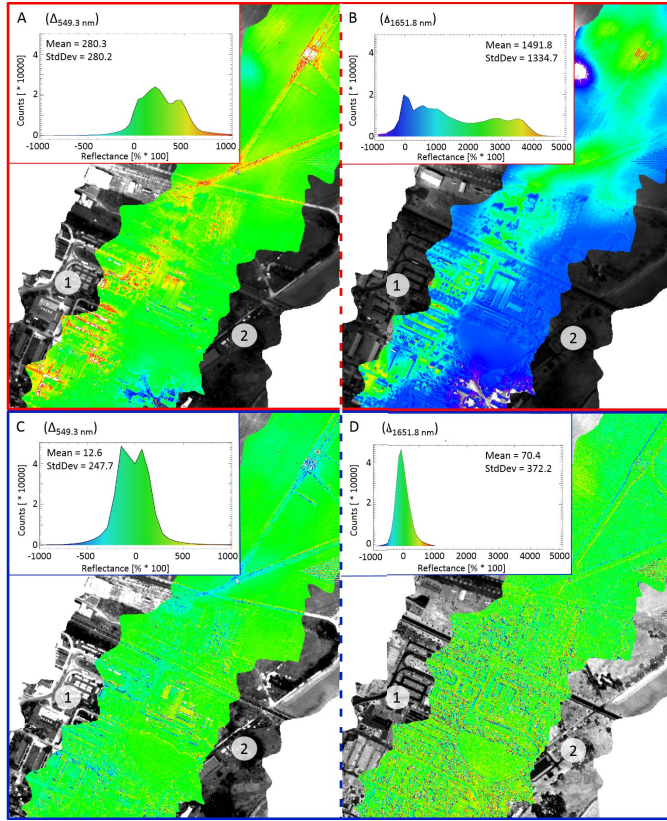


Fig. 14. Reflectance difference (color slice) between overlapping adjacent flight stripes (gray scale);  $\Delta$  = left flight stripe(1)-right flight stripe (2); histograms indicate the distribution of the resulting differences; Difference between uncorrected HSI reflectance (red border) for overlapping (a) 549.3- and (b) 1651.8-nm bands; Difference between cross-calibrated HSI reflectance (blue border) for overlapping (c) 549.3- and (d) 1651.8-nm bands.

cross-calibrated flight stripes [Fig. 14(c) and (d)] do not exhibit these patterns. The histograms and statistic assessments indicate a clear tendency toward smaller differences and a more homogeneous distribution. For the relatively short VNIR wavelength of 549.3 nm [Fig. 14(a) and (c)], minor reflectance differences caused by illumination are still perceptible due to the stronger diffuse scattering of smaller wavelengths. However, the overall tendency toward smaller differences is present. Especially for the SWIR wavelength [Fig. 14(b)], the illumination patterns are eliminated in the cross-corrected SWIR differences [Fig. 14(d)]. The spatial distribution indicates that only transition areas between surface objects are causing reflectance differences of  $\pm 3.7\%$  standard deviation. The comparison between the adjacent flight stripes indicates that across-track illumination gradients are compensated independent from shadow influence.

To assess the benefits for application and classification purposes, a supervised support vector machine (SVM) classification [33] has been carried out for the original HSI data [Fig. 15(a)] and the cross-calibrated data [Fig. 15(b)]. For the cross-calibrated data, the classification results in an overall accuracy of 98.56% and a kappa coefficient of 0.98. This contrasts with the overall accuracy of 78.79% and kappa coefficient of 0.71 for the original HSI data. The corrected data clearly show a classification improvement. Based on the

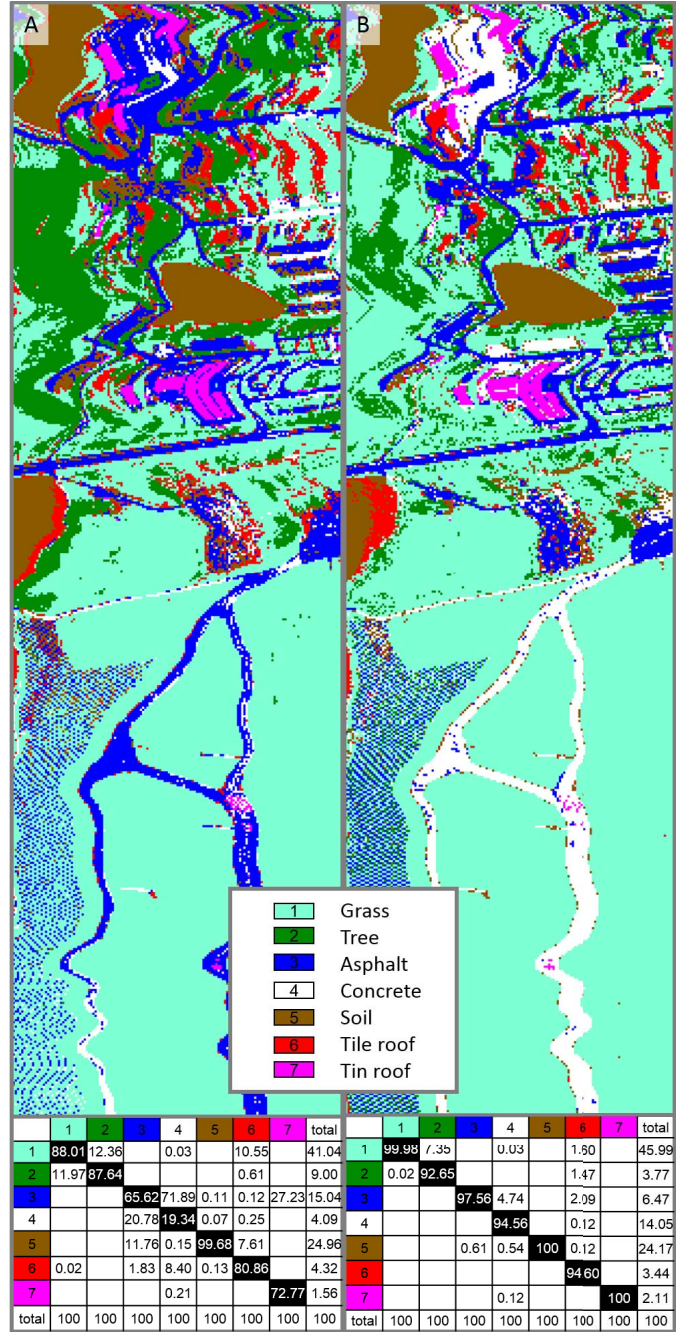


Fig. 15. Subsets (in sensor coordinates) of supervised SVM classification results (seven classes and three iterations) and their corresponding confusion matrix based on (a) reflectance without cross calibration and (b) cross-calibrated reflectance.

confusion matrix [Fig. 15(a)], it can be shown that for the original HSI data, concrete pixels are often falsely classified as asphalt and vice versa. In addition, grass surfaces are often misclassified as trees and vice versa. Also remarkable are the tin roofs, which are often falsely classified as asphalt. These misclassifications can be explained by a higher spectral similarity between these classes, especially under shadowed conditions. After the correction [Fig. 15(b); confusion matrix], misclassifications are significantly reduced, and the classifications of concrete, asphalt, trees, grass, and tin roofs especially profit from the corrections. Additional tests with a spectral

angle mapper (SAM) classification, usually more robust to variations of albedo, performed poorer for the corrected data and then SVM classification performed for the uncorrected data. The overall poorer SAM classification results for the uncorrected data also indicate nearly identical problems with the separation of trees and grass as well as with the separation of soil, asphalt, and concrete. These classification results imply that the cross-calibrated reflectance clusters representing certain surface objects are more separated and have smaller cluster variability. These are promising results for any type of more specialized application dealing with vegetation or urban classifications, where the influence of shadows always hampers the results.

## V. DISCUSSION

The results of the proposed illumination correction of the HSI data based on the cross calibration with the ALS intensity data seem promising for all urban and vegetation settings influenced by cast shadows. In addition, extreme complex illumination conditions, such as cloud or terrain shadowing, can be improved. A significant enhancement is indicated compared with the exclusive use of HSI data. The cross calibration is only a relative calibration; nevertheless, the combination has the potential to eliminate typically disturbing effects in passive sensor data. The benefits of compensating for illumination differences are evident when considering deshadowing, across-track illumination correction, albedo leveling, and mosaicking. With the active support, illumination changes over time beside shadow influences are compensated for. This is especially beneficial for the interpretation and classification of data acquired during long-lasting flight campaigns.

However, some requirements and assumptions considering the sensor systems, characteristics, and flight parameters have to be fulfilled to generate such results. The ray tracing-based approach is necessary to compensate for the influence of the different sensor responses, especially concerning tree canopies. Additional work must be performed to fulfill the requirements for an operational application in HSI data preprocessing. The overall radiative interaction between the sensors and various surface objects considering anisotropic behavior and roughness differences must be addressed. In addition, the sensor adaptation by filtering the point cloud should be evaluated in detail. In addition, the influence of the enhanced HSI data on more specific classification applications should be addressed in the future. The proposed method can be helpful, especially for the exploration of the different sensor responses. Due to the physically based adaptation, the method is generic and can be adapted to different ALS wavelengths. All of these efforts will profit from upcoming multiple-wavelength ALS systems and thereby bring airborne imaging spectroscopy closer to real reflectance measurement.

## VI. CONCLUSION

Three key findings can be drawn from the in-flight cross calibration of ALS and HSI sensors:

- 1) In general, deshadowing, illumination correction, albedo leveling, and mosaicking during HSI preprocessing can be enhanced using ALS intensity information.

- 2) As a consequence, classification can be improved by the fusion of intensity data from ALS and HSI. For example, the classification of heterogeneous urban and vegetated surfaces, which are spectrally confirmed under shadowed conditions, benefits from the data fusion.
- 3) A point-cloud-based combination and adaptation of both sensor responses on a raw data level is necessary, to properly characterize the morphological heterogeneity of vegetated and urban surfaces.

The proposed method is the first in-flight airborne HSI and ALS intensity data fusion. It is based on a rigorous radiometric correction of the ALS intensity data and cross calibration with the HIS data. The physically based correction results in realistic HSI reflectance values where relief, illumination, shadows, and directional effects have been compensated and corrected for. The method provides a suitable basis to explore and adapt the sensor responses and develop unexploited synergies concerning the radiometric enhancement of both sensors. The results show that a combination of active ALS and passive HSI systems can strengthen the overall data quality and classification accuracy of HSI reflectance, especially for heterogeneous vegetation structures and all urban settings. The data fusion is useful for complex illumination and shadowing situations, for example, clouds and rough terrain. The presented methodology and promising results can be applied for various specialized applications, such as tree-species identification and high-spatial resolution urban mapping, which rely on constant and comparable illumination conditions. Our results give evidence that, beyond the ALS accurate range measurement, these systems can support and enhance HSI preprocessing with intensity information, especially for heterogeneous urban and vegetation surface coverage. The combination of both sensors achieves a true reflectance measurement that accounts for shadowing, directional effects, and atmospheric heterogeneities. With future advances, such as multispectral ALS systems, a rigorous data fusion approach will be essential to extract high-resolution information and increase the quality of mapping applications.

## ACKNOWLEDGMENT

The authors would like to thank MILAN Geoservice GmbH, namely, D. Hannusch, for ALS instrumental, technical, and flight campaign support.

## REFERENCES

- [1] M. Dalponte, L. Bruzzone, and D. Gianelle, "Fusion of hyperspectral and LIDAR remote sensing data for classification of complex forest areas," *IEEE Trans. Geosci. Remote Sens.*, vol. 46, no. 5, pp. 1416–1427, May 2008.
- [2] G. P. Asner *et al.*, "Carnegie airborne observatory-2: Increasing science data dimensionality via high-fidelity multi-sensor fusion," *Remote Sens. Environ.*, vol. 124, pp. 454–465, Sep. 2012.
- [3] H. Buddenbaum, S. Seeling, and J. Hill, "Fusion of full-waveform LIDAR and imaging spectroscopy remote sensing data for the characterization of forest stands," *Int. J. Remote Sens.*, vol. 34, no. 13, pp. 4511–4524, 2013.
- [4] M. Alonso, B. Bookhagen, and D. A. Roberts, "Urban tree species mapping using hyperspectral and LIDAR data fusion," *Remote Sens. Environ.*, vol. 148, pp. 70–83, May 2014.
- [5] U. Heiden, W. Heldens, S. Roessner, K. Segl, T. Esch, and A. Mueller, "Urban structure type characterization using hyperspectral remote sensing and height information," *Landscape Urban Planning*, vol. 105, no. 4, pp. 361–375, Apr. 2012.

- [6] Y. Gu, Q. Wang, X. Jia, and J. A. Benediktsson, "A novel MKL model of integrating LIDAR data and MSI for urban area classification," *IEEE Trans. Geosci. Remote Sens.*, vol. 53, no. 10, pp. 5312–5326, Oct. 2015.
- [7] G. P. Asner *et al.*, "Carnegie airborne observatory: In-flight fusion of hyperspectral imaging and waveform light detection and ranging for three-dimensional studies of ecosystems," *J. Appl. Remote Sens.*, vol. 1, no. 1, p. 013536, Sep. 2007.
- [8] T. U. Kampe, "NEON: The first continental-scale ecological observatory with airborne remote sensing of vegetation canopy biochemistry and structure," *J. Appl. Remote Sens.*, vol. 4, no. 1, p. 043510, Mar. 2010.
- [9] M. Brell, C. Rogass, K. Segl, B. Bookhagen, and L. Guanter, "Improving sensor fusion: A parametric method for the geometric coalignment of airborne hyperspectral and LIDAR data," *IEEE Trans. Geosci. Remote Sens.*, vol. 54, no. 6, pp. 3460–3474, Jun. 2016.
- [10] H. Torabzadeh, F. Morsdorf, and M. E. Schaepman, "Fusion of imaging spectroscopy and airborne laser scanning data for characterization of forest ecosystems—A review," *ISPRS J. Photogramm. Remote Sens.*, vol. 97, pp. 25–35, Nov. 2014.
- [11] Q. Zhang, V. P. Pauca, R. J. Plemmons, and D. D. Nikic, "Detecting objects under shadows by fusion of hyperspectral and LIDAR data: A physical model approach," in *Proc. 5th Workshop Hyperspectral Image Signal Process., Evol. Remote Sens.*, 2013, pp. 1–4.
- [12] E. J. Ientilucci, "Leveraging LIDAR data to aid in hyperspectral image target detection in the radiance domain," in *SPIE Def. Secur., and Sens.*, pp. 839007-1–839007-12, 2012.
- [13] A. Roncat, C. Briese, and N. Pfeifer, "A comparison of LIDAR reflectance and radiometrically calibrated hyperspectral imagery," *ISPRS-Int. Arch. Photogramm., Remote Sens. Spatial Inf. Sci.*, vol. XLI-B7, pp. 705–710, Jun. 2016.
- [14] P. J. Hartzell *et al.*, "Comparison of synthetic images generated from LIDAR intensity and passive hyperspectral imagery," in *Proc. IEEE Int. Geosci. Remote Sens. Symp. (IGARSS)*, Jul. 2014, pp. 1345–1348.
- [15] S. Hagstrom and J. Broadwater, "Generating passive NIR images from active LIDAR," in *Proc. SPIE 9832, Laser Radar Technol. App.*, p. 98320G, May 2016.
- [16] J. U. H. Etel *et al.*, "Beyond 3-D: The new spectrum of LIDAR applications for earth and ecological sciences," *Remote Sens. Environ.*, vol. 186, pp. 372–392, Dec. 2016.
- [17] D. Schläpfer, R. Richter, and A. Damm, "Correction of shadowing in imaging spectroscopy data by quantification of the proportion of diffuse illumination," in *Proc. 8th SIG-EARSeL Imag. Spectrosc. Workshop Nantes*, 2013, p. 10.
- [18] C. Briese, M. Pfennigbauer, H. Lehner, A. Ullrich, W. Wagner, and N. Pfeifer, "Radiometric calibration of multi-wavelength airborne laser scanning data," *ISPRS Ann. Photogramm., Remote Sens. Spatial Inf. Sci.*, vol. 1, no. 7, pp. 335–340, 2012.
- [19] W. Wagner, "Radiometric calibration of small-footprint full-waveform airborne laser scanner measurements: Basic physical concepts," *ISPRS J. Photogramm. Remote Sens.*, vol. 65, no. 6, pp. 505–513, Nov. 2010.
- [20] F. Coren and P. Sterzai, "Radiometric correction in laser scanning," *Int. J. Remote Sens.*, vol. 27, no. 15, pp. 3097–3104, Aug. 2006.
- [21] A. G. Kashani, M. J. Olsen, C. E. Parrish, and N. Wilson, "A review of LIDAR radiometric processing: From ad hoc intensity correction to rigorous radiometric calibration," *Sensors*, vol. 15, no. 11, pp. 28099–28128, Nov. 2015.
- [22] *HySpex, Norsk Elektro Optikk*, accessed on May 19, 2015. [Online]. Available: <http://www.hyspex.no/index.php>
- [23] K. Lenhard, A. Baumgartner, and T. Schwarzmaier, "Independent laboratory characterization of NEO HySpex imaging spectrometers VNIR-1600 and SWIR-320m-e," *IEEE Trans. Geosci. Remote Sens.*, vol. 53, no. 4, pp. 1828–1841, Apr. 2015.
- [24] *RIEGL—RIEGL Laser Measurement Systems*, accessed on May 19, 2015. [Online]. Available: <http://www.riegl.com/>
- [25] W. Wagner, A. Ullrich, V. Ducic, T. Melzer, and N. Studnicka, "Gaussian decomposition and calibration of a novel small-footprint full-waveform digitising airborne laser scanner," *ISPRS J. Photogramm. Remote Sens.*, vol. 60, no. 2, pp. 100–112, Apr. 2006.
- [26] L. Guanter, K. Segl, B. Sang, L. Alonso, H. Kaufmann, and J. Moreno, "Scene-based spectral calibration assessment of high spectral resolution imaging spectrometers," *Opt. Exp.*, vol. 17, no. 14, pp. 11594–11606, Jul. 2009.
- [27] R. Richter, T. Kellenberger, and H. Kaufmann, "Comparison of topographic correction methods," *Remote Sens.*, vol. 1, no. 3, pp. 184–196, Jul. 2009.
- [28] L. Guanter, K. Segl, and H. Kaufmann, "Simulation of optical remote-sensing scenes with application to the EnMAP hyperspectral mission," *IEEE Trans. Geosci. Remote Sens.*, vol. 47, no. 7, pp. 2340–2351, Jul. 2009.
- [29] A. Berk *et al.*, "MODTRAN cloud and multiple scattering upgrades with application to AVIRIS," *Remote Sens. Environ.*, vol. 65, no. 3, pp. 367–375, Sep. 1998.
- [30] M. Alonso, B. Bookhagen, J. P. McFadden, A. Sun, and D. A. Roberts, "Mapping urban forest leaf area index with airborne LIDAR using penetration metrics and allometry," *Remote Sens. Environ.*, vol. 162, pp. 141–153, Jun. 2015.
- [31] A. Clasen *et al.*, "Spectral unmixing of forest crown components at close range, airborne and simulated Sentinel-2 and EnMAP spectral imaging scale," *Remote Sens.*, vol. 7, no. 11, pp. 15361–15387, Nov. 2015.
- [32] S. Roessner, K. Segl, U. Heiden, and H. Kaufmann, "Automated differentiation of urban surfaces based on airborne hyperspectral imagery," *IEEE Trans. Geosci. Remote Sens.*, vol. 39, no. 7, pp. 1525–1532, Jul. 2001.
- [33] C.-C. Chang and C.-J. Lin, "LIBSVM: A library for support vector machines," *ACM Trans. Intell. Syst. Technol.*, vol. 2, no. 3, pp. 27:1–27:27, 2011. [Online]. Available: <http://www.csie.ntu.edu.tw/~cjlin/libsvm>



**Maximilian Brell** received the Diploma degree in geography from the Dresden University of Technology, Dresden, Germany, in 2011. His Ph.D. thesis is on airborne hyperspectral imaging and LiDAR sensor fusion.

He was a Research Assistant with the Remote Sensing Section, Helmholtz Centre Potsdam, GFZ German Research Centre for Geoscience, Potsdam, Germany. He developed a preprocessing chain for airborne hyperspectral data.



**Karl Segl** received the Doctorate degree from the Faculty of Engineering, University of Karlsruhe, Karlsruhe, Germany, in 1996.

He is currently a Team Leader of the EO Mission Development and Data Processing Group with the Remote Sensing Section, GFZ German Research Centre for Geosciences, Potsdam, Germany. He has more than 25 years of experience in the field of imaging spectroscopy and teaches remote sensing at the University of Potsdam, Potsdam. His research interests include new methodological developments for imaging spectroscopy, sensor simulation, sensor design, and big data.



**Luis Guanter** received the Ph.D. degree in environmental physics from the University of Valencia, Valencia, Spain, in 2007.

He has held postdoctoral positions at the German Research Center for Geosciences (GFZ) Potsdam, Potsdam, Germany, the Freie Universität Berlin, Berlin, Germany, and Oxford University, Oxford, U.K., as an EC Marie Curie Fellow. Since 2012, he has been leading the DFG Emmy Noether Junior Research Group on chlorophyll fluorescence monitoring. Since 2014, he has also been the Leader of the Remote Sensing Section with the Helmholtz Center Potsdam, GFZ, in a joint appointment professorship position with the Institute of Earth and Environmental Science of the University of Potsdam, Potsdam. He is currently the Scientific Principle Investigator with the EnMAP Hyperspectral Mission, Bremen, Germany. His research interests include the monitoring of land and atmospheric processes through imaging spectroscopy.

Dr. Guanter is a member of the Advisory Board of other satellite missions.



**Bodo Bookhagen** received the Diploma degree in geology and the doctor's degree (*summa cum laude*) in geoscience from the University of Potsdam, Potsdam, Germany, in 2000 and 2005, respectively.

He was a Postdoctoral Researcher with the University of California, Berkeley, CA, USA, Stanford University, Stanford, CA, USA, and the University of California, Santa Barbara, CA, USA. From 2007 to 2014, he was an Assistant Professor and an Associate Professor at the University of California, Santa Barbara. Since 2014, he has been the Chair of Geological Remote Sensing at the University of Potsdam.